Nano Research

Open Access

Research Article

High-entropy alloy nanosheets engineered aptasensor for ultrasensitive detection of pro gastrin releasing peptide in small-cell lung cancer

Imamdin Chandio[1], Yongjian Ai[2]✉, and Qionglin Liang[1]✉

[1] *MOE Key Laboratory of Bioorganic Phosphorus Chemistry & Chemical Biology, Department of Chemistry, Laboratory of Flexible Electronics Technology, Center for Synthetic and Systems Biology, Tsinghua University-Peking University Joint Centre for Life Sciences, Tsinghua University, Beijing 100084, China*

[2] *MOE Key Laboratory of Precision Nutrition and Food Quality, Department of Nutrition and Health, China Agricultural University, Beijing 100193, China*

Cite this article: *Nano Research*, **2026**, *19*, 94908352. https://doi.org/10.26599/NR.2026.94908352

ABSTRACT: Small-cell lung cancer (SCLC) is an aggressive malignancy characterized by rapid progression, early metastasis, and poor prognosis. These features highlight the urgent need for ultrasensitive and non-invasive diagnostic methods. Pro-gastrin-releasing peptide (ProGRP) has emerged as a highly specific biomarker for SCLC. However, existing detection techniques are often limited by long assay times and insufficient sensitivity. In this study, we developed a new electrochemical aptasensor based on two-dimensional high-entropy alloy nanosheets (HEANSs) for ultra-precise detection of ProGRP. The HEANSs were synthesized via a salt-templated method, which enabled precise control over composition, enhanced catalytic activity due to lattice distortion, and a uniform nanosheet morphology with high surface area. The HEANSs were functionalized with polydopamine (PDA), thereby introducing a variety of reactive functional groups that improved biocompatibility and markedly enhanced the efficiency of aptamer immobilization. This synergistic design achieved a broad linear detection range from 10 pg/mL to 100 μg/mL, an ultra-low limit of detection (LOD) of 0.874 pg/mL (S/N = 3), and excellent reproducibility with a relative standard deviation (RSD) of 1.78%. Moreover, the sensor retained 3.75% of its initial signal after nine days of storage, demonstrating exceptional stability. This pioneering HEANSs@PDA-based aptasensor provides a scalable and versatile platform for ultrasensitive biomarker detection, holding significant potential for early cancer diagnosis, real-time clinical monitoring, and precision medicine applications.

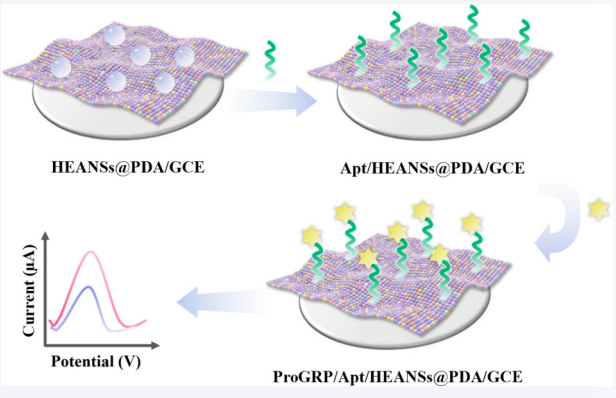

KEYWORDS: high-entropy alloy nanosheets (HEANSs), polydopamine functionalization, electrochemical aptasensor, pro-gastrin-releasing peptide (ProGRP), salt-templated synthesis

1 Introduction

Lung cancer (LC) remains a major global health burden, representing one of the leading causes of cancer-related morbidity and mortality worldwide. According to recent epidemiological reports, LC accounts for approximately 12.4% of all newly diagnosed cancers and contributes to nearly 18.7% of global cancer-related deaths, reflecting its aggressive nature and limited therapeutic success rates. Clinically, LC is broadly classified into two major histological subtypes: small-cell lung cancer (SCLC) and non-small-cell lung cancer (NSCLC). NSCLC constitutes the predominant form, accounting for ~ 85% of all cases, whereas SCLC represents the remaining 15%. Despite its lower incidence, SCLC is characterized by rapid tumor growth, early dissemination, and poor prognosis, making it one of the most lethal malignancies. The high recurrence rate, limited therapeutic options, and frequent development of chemoresistance further underscore the urgent need for early and precise diagnostic strategies tailored to SCLC

Received: November 11, 2025; **Revised:** December 13, 2025
Accepted: December 16, 2025

✉Address correspondence to Yongjian Ai, ayj@tsinghua.edu.cn; Qionglin Liang, Liangql@tsinghua.edu.cn

management [1–3]. Despite its lower incidence, SCLC is an aggressive malignancy characterized by rapid tumor growth, early metastasis, and poor prognosis [4, 5]. Current therapeutic approaches for SCLC, primarily comprising chemotherapy, radiotherapy, and, in select cases, surgical resection, remain largely palliative, offering only transient disease control. Although many patients respond initially, resistance typically emerges rapidly, leading to disease relapse and underscoring the critical need for new and more effective therapeutic approaches [6–9]. Consequently, early detection and continuous disease monitoring are essential for improving survival outcomes. However, conventional diagnostic methods, including histopathological and cytological evaluation of tissue specimens, are invasive, challenging to perform repeatedly, and often unsuitable for patients with compromised health conditions [10, 11]. These limitations have driven growing interest in liquid biopsy, a minimally invasive diagnostic strategy that enables the detection of circulating tumor biomarkers, such as DNA, RNA, and proteins from peripheral blood [12, 13]. Among these serum biomarkers, ProGRP has gained prominence as a more reliable and specific indicator for SCLC diagnosis. ProGRP is more stable in peripheral circulation, correlates closely with treatment response, and exhibits significantly elevated levels in patients with extensive-stage disease [14–17]. Several methods, including enzyme-linked immunosorbent assay (ELISA) [18]. Liquid chromatography–mass spectrometry (LC–MS) [19], and a molecularly imprinted polymer (MIP)-based assay have been developed for ProGRP detection. However, these conventional techniques are often limited by high costs, long processing times, and inadequate sensitivity. To overcome these challenges, electrochemical biosensors have gained significant attention as a promising diagnostic device, offering rapid detection, high sensitivity, cost-effectiveness, and operational simplicity [20–22]. Aptamer-based electrochemical platforms enhanced by nanomaterial-driven signal amplification have emerged as highly effective tools for sensitive biomarker detection [23–25]. Aptamers, single-stranded oligonucleotides generated through systematic evolution of ligands by exponential enrichment (SELEX), provide high affinity, chemical stability, and ease of modification. Compared to antibodies, aptamers are chemically synthesized, non-immunogenic, and easily modified, displaying superior thermal stability, making them highly suitable for biosensing applications [26–29]. Advanced nanomaterials play a pivotal role in biosensor development by offering high surface areas, superior electrical conductivity, and versatile catalytic properties, collectively enabling next-generation devices with enhanced sensitivity, selectivity, and real-time diagnostic performance [30–35]. The rising demand for high-performance sensing materials has increasingly drawn attention to high-entropy alloys (HEAs), an emerging class of multicomponent systems first formally introduced by Yeh et al. in 2004, due to their unique structural features and tunable physicochemical properties [36]. HEAs consist of five or more metallic elements in near-equimolar proportions, and their inherently high configurational entropy promotes the stabilization of single-phase solid solutions with unique structural and functional advantages. Consequently, HEAs exhibit remarkable thermal stability, strong corrosion resistance [37–39], and highly tunable electronic structures, further enhancing their suitability for advanced sensing and catalytic applications [40–42]. Owing to these advantages, HEANSs have recently attracted considerable attention for biosensing applications due to their large active surface area, abundant catalytic sites, and excellent electron-transfer properties [43–47]. Despite these promising attributes, challenges persist regarding the control of reactivity, colloidal stability, and surface functionalization of HEANSs. To address these limitations, PDA, a bioinspired polymer formed through the self-polymerization of dopamine (DA), offers an effective strategy by uniformly coating the nanosheets and introducing abundant catechol and amine functional groups. These surface functionalities enhance dispersibility, facilitate efficient biomolecule immobilization, and improve biocompatibility, all while preserving the intrinsic electrochemical performance of the HEANSs. The resulting HEANSs@PDA form a hybrid material that combines the catalytic and structural advantages of HEANSs with the bio-interactive functional groups of PDA, offering new opportunities for biosensing and biomedical applications [48–50].Various approaches have been explored for HEA nanomaterial synthesis, including solid-state reactions, ball milling, carbothermal shock, solvothermal techniques, and co-precipitation, each offering distinct advantages and limitations in terms of compositional control, scalability, and structural uniformity, and these techniques require high temperatures (> 900 °C) and specialized equipment, often resulting in heterogeneous morphology and low surface area [51–53]. To address these limitations, the salt-templated strategy enabled the scalable fabrication of ultrathin HEANSs with uniform morphology [54]. In this process, a mixture of metal salts is reduced in a molten salt matrix under a controlled atmosphere, enabling uniform nucleation, morphology control, and compositional homogeneity while preventing particle aggregation. This approach allows the scalable production of nanosheets and nanostructures with high surface area, ideal for electrochemical and optical biosensors. By combining salt-templated synthesis with compositional engineering, HEANSs can be precisely tailored to enhance biomolecule immobilization, sensitivity, and stability, advancing their application in early disease diagnostics, clinical monitoring, and environmental detection.

Herein, we developed an electrochemical aptasensor based on HEANSs@PDA for the ultrasensitive detection of ProGRP, a critical biomarker for SCLC. The salt-templated synthesis enabled the production of uniform 2D HEANSs with abundant electroactive sites, while PDA functionalization introduced bioactive groups that significantly improved aptamer immobilization and biocompatibility. The resulting aptasensor exhibits a broad linear detection range from 10 pg/mL to 100 μg/mL, an ultra-low LOD of 0.874 pg/mL (S/N = 3), and outstanding precision, demonstrated by an RSD of 1.78%. Furthermore, the sensor maintains excellent stability, retaining over 3.75% of its initial signal after nine days of storage (Scheme 1). This work highlights the potential of high-entropy nanomaterials in advanced biosensing applications and introduces a versatile platform for the development of next-generation diagnostic devices.

2 Experimental section

2.1 Reagents

The chemicals, $Ni(acac)_2$ (AR, ≥ 99%), $Cu(acac)_2$ (AR, ≥ 98%), $Co(acac)_2$ (AR, ≥ 98%–99%), $Ir(acac)_2$ (AR, ≥ 99%), and $Fe(acac)_2$ (AR, ≥ 99%) were purchased from Tanfeng Tech. Co., Ltd. (China), sodium chloride (NaCl, ≥ 99.99%), potassium ferricyanide ($K_3Fe(CN)_6$, 99%), and potassium ferrocyanide ($K_4Fe(CN)_6{\cdot}3H_2O$, ≥

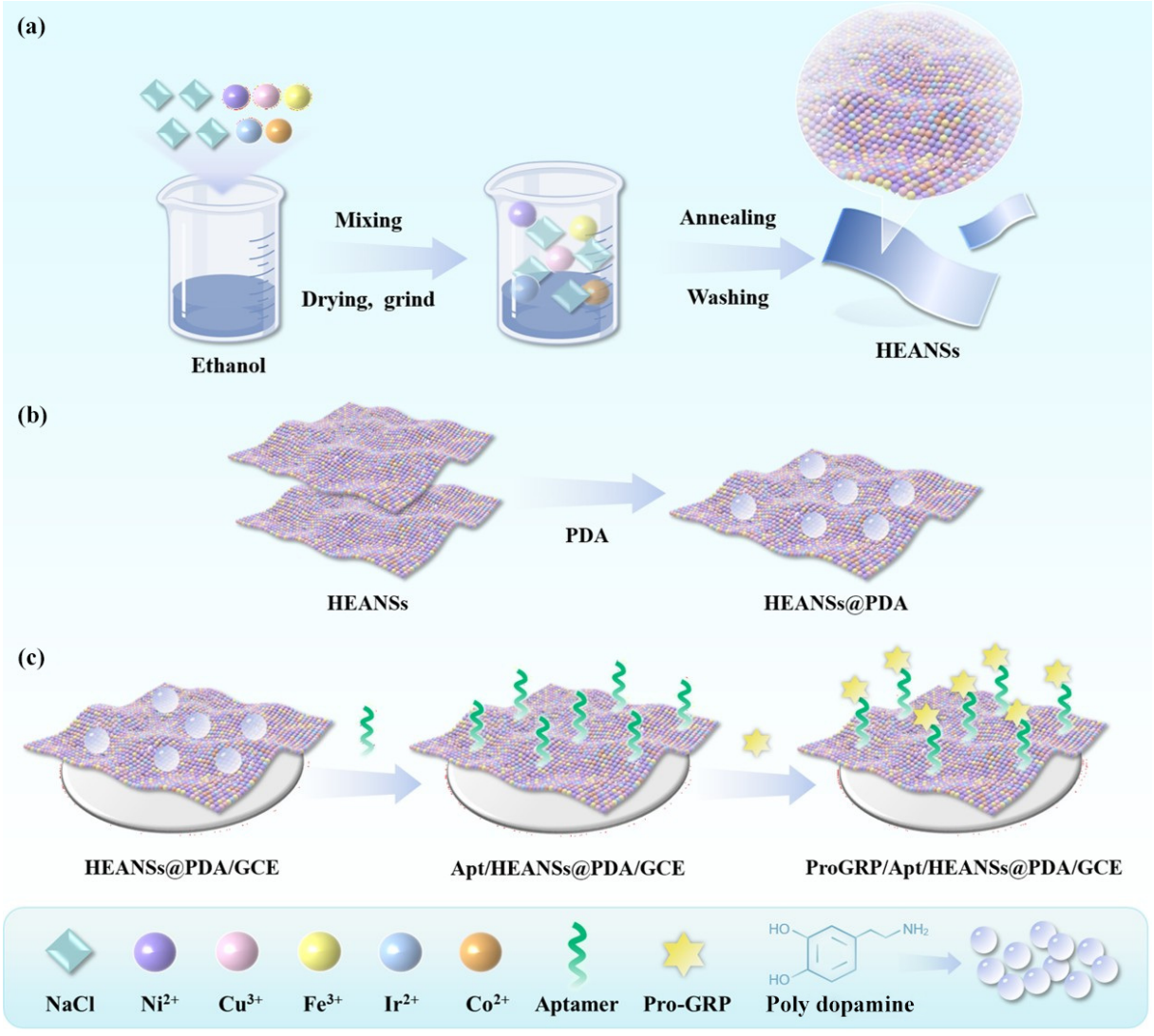

Scheme 1 Schematic representation of the overall fabrication process, including the synthesis of HEANSs (a), their surface functionalization with PDA (b), and the subsequent stepwise immobilization of the aptamer and ProGRP on the HEANSs@PDA/GCE (c).

98.5%) were purchased from Shanghai Macklin Biochemical Co., Ltd. (China). Phosphate buffer solution (PBS, 0.1 mmol, pH 7.4) was bought from Sangon Biotech Co., Ltd. (China). Potassium chloride (KCl, 99%) and ethanol (CH_3CH_2OH, 99%) were taken from Beijing Chemical Plant (China). The modified NH_2-aptamer with the sequence of 5'-NH_2-GGTTGGTGTGGTTGG-3' was designed and improved accordingly [55]. Carcinoembryonic antigen (CEA), calprotectin (CP), prostate-specific antigen (PSA), ProGRP 31-98, and Alpha-fetoprotein (AFP) were also obtained by Sangon Biotechnology (China). The Milli-Q water purification system was used for water in the whole experiment.

2.2 Experimental framework

Electrochemical tests were conducted using a conventional three-electrode setup on a CHI 440 electrochemical workstation (Shanghai CH Instruments Co., China). The working electrode (WE) was a modified bare glassy carbon electrode (BGCE, 3 mm in diameter), the counter electrode (CE) was a platinum wire, and the reference electrode (RE) was an Ag/AgCl electrode. Scanning electron microscopy equipped with energy dispersive X-ray spectroscopy (SEM-EDS), transmission electron microscopy (TEM) was performed using a JEOL JSM-6700F microscope, while high-resolution transmission electron microscopy (HRTEM) analysis was conducted using a JEOL JEM-2100F microscope. Atomic force microscopy (AFM) measurements were conducted using a Bruker Dimension Icon system in tapping mode. An X-ray photoelectron spectroscopy (XPS) study was carried out by applying a PHI Quantera SXM spectrometer. Fourier transform infrared (FT-IR) spectroscopy analysis was performed using a Bruker FT-IR spectrometer (Germany). Brunauer–Emmett–Teller (BET) and X-ray diffraction (XRD) analyses were carried out using a DX-2700 diffractometer.

2.3 Fabrication of HEANSs

The synthesis of HEANSs by using the salt-templating method involves a two-step process comprising high-temperature annealing and subsequent salt removal. In a typical synthesis, 0.6 mmol of each metal precursor $Fe(acac)_2$, $Co(acac)_2$, $Cu(acac)_2$, $Ni(acac)_2$, and $Ir(acac)_2$ was dissolved in 60 mL of ethanol under magnetic stirring for 30 min to form a homogeneous solution. Subsequently, 60 g of NaCl powder was added, and the mixture was stirred vigorously for 48 h at room temperature to ensure a uniform dispersion. The

resulting mixture was dried at 60 °C and finely ground using a mortar and pestle. The powder was then subjected to annealing at 800 °C for 2 h under a nitrogen (N_2) atmosphere. Finally, the annealed product was thoroughly washed with deionised (DI) water to remove the NaCl template, yielding ultra-thin HEANSs completely. The Fe, Co, Cu, Ni, and Ir elements were selected due to their complementary catalytic activity, redox properties, and electronic conductivity, which collectively support high sensitivity and selectivity in biosensing. Their integration into an HEA matrix generates strong multicomponent synergy, resulting in enhanced surface reactivity, structural stability, and electrochemical performance. The inherent lattice distortion and compositional complexity of HEANSs further increase active site density and durability, making them highly suitable for advanced sensing applications [56–59].

2.4 Modification of HEANSs with PDA

The surface of HEANSs was functionalized first time with PDA coating through PDA under alkaline conditions. Briefly, HEANSs (10 mg) were dispersed in 50 mL of Tris-HCl buffer solution (10 mM, pH 8.5) via ultrasonication for 30 min to achieve a stable suspension. Dopamine hydrochloride ($C_8H_{12}ClNO_2$, 20 mg) was then added to the dispersion, and the mixture was gently stirred at room temperature for 12 h, allowing PDA to undergo oxidative self-polymerization and deposit as a thin PDA layer on the nanosheet surfaces. The resulting HEANSs@PDA were collected by centrifugation, thoroughly washed several times with DI water and ethanol to remove excess DA and by-products, and dried under vacuum for subsequent characterization and application.

2.5 Fabrication of HEANSs@PDA based sensor

Before modification, the GCE was consecutively washed with alumina slurries of 0.1, 0.3, and 0.5 μm on a cleaning pad to confirm a mirror-like clean surface. These electrodes were carefully cleaned with a solution of DI water and ethanol, followed by ultrasonication for five min to remove any residual particulates. After washing, the electrodes were dried under a gentle stream of N_2 gas. Then, 8 μL of the suspension of HEANSs@PDA was carefully poured dropwise onto its surface and allowed to dry at room temperature to form HEANSs@PDA/GCE. Subsequently, 9 μL of an aptamer solution (3.5 μM in 0.1 mM PBS, pH 7.4) was deposited on the modified electrode surface and incubated for 45 min at room temperature, resulting in the formation of Apt/HEANSs@PDA/GCE probe. The modified electrode was rinsed gently with PBS to remove any non-specifically adsorbed aptamer molecules. The fabricated aptasensor was stored at 4 °C until use. For target detection, 20 μL of ProGRP solution (10 ng/mL) was introduced to the surface of the probe, then incubated for 40 min, allowing specific aptamer–protein binding.

2.6 Electrochemical analysis

The aptasensor was characterized after each functionalization step by cyclic voltammetry (CV), differential pulse voltammetry (DPV), and electrochemical impedance spectroscopy (EIS). All tests were performed in 5 mM $[Fe(CN)_6]^{3-/4-}$ containing 0.1 M KCl. CV was recorded between −0.1 and 0.7 V at 100 mV/s, DPV between −0.1 and 0.7 V, and EIS at an open-circuit potential (OCP) of 0.27 V over a frequency range of 10^2 to 10^6 Hz (amplitude 5 mV). Specific ProGRP binding was indicated by a reduced peak current and increased charge-transfer resistance, demonstrating hindered electron and mass transfer after the biomarker bound. To the best of our knowledge, this work is the first to pioneer the use of HEANSs@PDA as an innovative platform for highly sensitive and reliable electrochemical detection of ProGRP, offering a groundbreaking pathway for early diagnosis and clinical monitoring.

3 Results and discussion

3.1 Characterization of the HEANSs@PDA sensor

The morphology, elemental distribution, and surface characteristics of HEANSs were thoroughly analyzed using SEM-EDS, TEM, HRTEM-EDS, and AFM. SEM analysis (Fig. 1(a)) revealed the surface morphology and particle distribution, while the corresponding SEM-EDS mapping (Fig. S1 in the Eletronic Supplementary Material (ESM)) confirmed the elemental composition. The material displayed a well-defined sheet-like architecture, indicative of the successful fabrication of porous nanosheets. The TEM image (Fig. 1(b)) reveals ultrathin nanosheets with a well-defined layered architecture, indicative of nanoscale thickness and structural uniformity. The smooth surface morphology, accompanied by regions of darker contrast, can be attributed to local variations in thickness or mass density. HRTEM-EDS elemental mapping analysis, showing the homogeneous distribution of multiple metal elements (Cu, Fe, Co, Ni, and Ir) throughout the nanosheets (Fig. 1(c)). Each element is uniformly dispersed, which is a key feature of multicomponent or high-entropy materials, ensuring consistent electronic and catalytic properties. The EDS survey analysis, along with its corresponding quantitative analysis of elemental composition (Figs. 1(d) and 1(e)), which contains Cu (65.7 wt.%), Fe (11.1 wt.%), Co (8.6 wt.%), Ni (8.1 wt.%), and Ir (6.5 wt.%), confirming the successful incorporation of all five elements in near-equimolar proportions and demonstrating that each element is evenly distributed across the nanosheet matrix. The uniform elemental distribution and high-resolution peaks indicate successful synthesis of HEANSs. An AFM image offering high-resolution characterization of surface topography (Figs. 1(f) and 1(g)). The nanosheets exhibit an ultrathin structure with lateral dimensions of approximately 3.7 ± 0.7 nm. These ultrathin characteristics of nanosheets are beneficial for increasing active surface sites. Nitrogen adsorption–desorption (BET) analysis at 77 K (Fig. 1(g)) displays a substantial improvement in the textural properties of the HEANSs after NaCl removal. Before the removal of NaCl (CuFeCoNiIr-NaCl), the material exhibits a low surface area (48.2 m^2/g), minimal pore volume (0.052 cc/g), and a relatively large average pore diameter (2.74 nm), indicating obstructed or insufficiently developed porosity. Upon removal of NaCl, (CuFeCoNiIr), the surface area increases sharply to 259.97 m^2/g, accompanied by a significant rise in pore volume to 0.64 cc/g and a slight decrease in pore diameter to 2.19 nm, confirming the formation of a well-developed porous structure. This transformation indicates the development of a well-defined mesoporous structure with abundant accessible active sites. The significant increase in surface area and porosity is attributed to the salt-templating synthesis strategy, where NaCl acts as a removable scaffold to support the formation of ultra-thin 2D nanosheets. Upon removal, the exposed nanosheet architecture provides a high density of mesopores, improving surface accessibility and mass transport pathways, which are critical for catalytic and electrochemical applications. Thus, this study

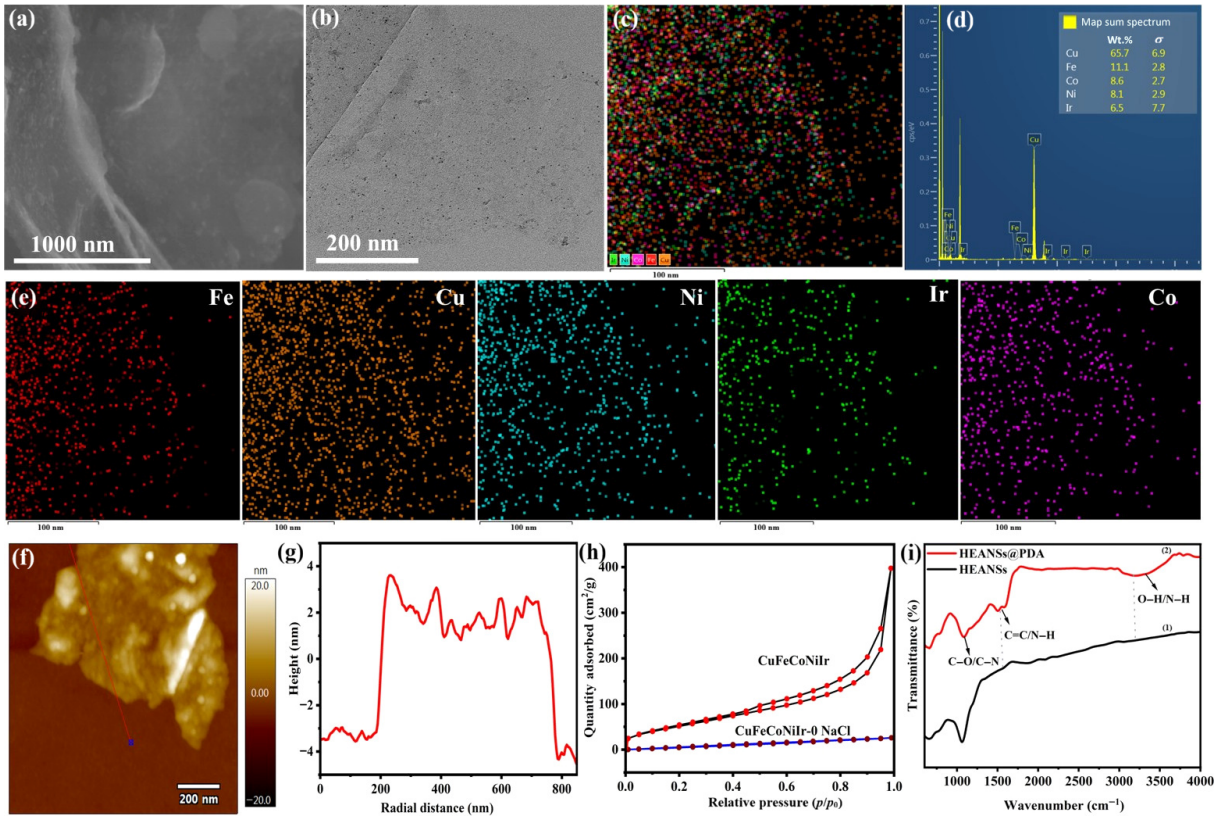

Figure 1 SEM image (a), TEM image (b), HRTEM–EDS images (c)–(e), AFM image (f) and (g), BET curves (h), and FT-IR spectra (i) analyses provide complementary insights into the morphology, elemental distribution, surface topography, porosity, and successful incorporation of PDA within HEANSs.

highlights that NaCl-assisted synthesis followed by template removal is a highly effective approach for tailoring the textural properties of HEANSs. FT-IR spectroscopy was employed to investigate the surface modification of HEANSs before and after PDA functionalization. The FT-IR analysis of pristine HEANSs exhibits no significant broad transmittance peaks, indicating minimal organic species attached to the nanosheet surfaces (Fig. 1(i), curve (1)). In contrast, after PDA functionalization, multiple characteristic absorption bands appear in the HEANSs@PDA spectrum (Fig. 1(i), curve (2)). Notably, peaks observed in the ~ 1100–1300 cm^{-1} range correspond to C=O and C–N stretching vibrations, the peaks appearing at ~ 1500–1600 cm^{-1} are attributed to C=C and N–H vibrations, and the broad band around ~ 3300–3500 cm^{-1} is associated with O–H and N–H stretching groups. The emergence of these additional peaks confirms the successful PDA modification on the surface of HEANSs, which introduces abundant functional groups and enhances surface activity, thereby enabling aptamer immobilization for biosensing applications.

The XPS was employed to investigate the elemental composition of HEANSs@PDA, thereby confirming the successful fabrication and surface functionalization of HEANSs. The survey spectrum (Fig. 2(a)) clearly reveals the presence of Co, Ir, Fe, Cu, Ni, O, N, and C, demonstrating the incorporation of all constituent elements and their uniform distribution across the nanosheets. The well-defined peaks and distinct satellite feature further suggest strong electronic interactions within the HEA matrix. High-resolution spectra of individual elements provided detailed insights into their chemical states. The Co 2p spectrum (Fig. 2(b)) exhibited two characteristic peaks at ~ 780 (Co $2p_{3/2}$) and ~ 795 eV (Co $2p_{1/2}$), consistent with Co species in the alloy. The Ir 4f region (Fig. 2(c)) displayed peaks at ~ 61.5 (Ir $4f_{7/2}$) and ~ 64.5 eV (Ir $4f_{5/2}$), confirming the presence of metallic Ir. For Fe (Fig. 2(d)), peaks at ~ 710.8 (Fe $2p_{3/2}$) and ~ 724.5 eV (Fe $2p_{1/2}$) indicated the coexistence of Fe^{2+} and Fe^{3+} states, suggesting surface heterogeneity and the potential for enhanced catalytic activity. Similarly, the Cu 2p spectrum (Fig. 2(e)) showed a main peak at ~ 932.5 eV (Cu $2p_{3/2}$) and a corresponding peak at ~ 952.5 eV (Cu $2p_{1/2}$), confirming the coexistence of Cu^{+} and Cu^{2+} species. The Ni 2p spectrum (Fig. 2(f)) revealed peaks at ~ 855.5 (Ni $2p_{3/2}$) and ~ 873.2 eV (Ni $2p_{1/2}$), attributed to Ni^{2+}, along with higher-energy components corresponding to Ni^{3+}. The non-metallic components further confirmed successful PDA functionalization. The O 1s spectrum (Fig. 2(g)) was deconvoluted into peaks at ~ 533.5 (–OH), 532.2 (C–O), and 531.0 eV (C=O), originating from catechol and quinone moieties in PDA. The N 1s spectrum (Fig. 2(h)) exhibited signals at ~ 400.3 (C–N), 399.3 (C–NH_2), and a minor peak near ~ 401.5 eV (–NH–), consistent with the nitrogen-rich structure of PDA. Meanwhile, the C 1s spectrum (Fig. 2(i)) showed dominant peaks at 284.8 (C–C/C=C), 286.2 (C–N/C–O), and 288.1 eV (C=O), reflecting the aromatic polymer backbone derived from dopamine. Altogether, the XPS results confirm that the HEANSs are composed of multiple transition metals with mixed oxidation states, while the surface is successfully incorporated with PDA. The abundant oxygen- and nitrogen-containing functional groups introduced by PDA enhance hydrophilicity, colloidal stability, and surface reactivity, rendering HEANSs@PDA well suited for biosensing applications.

The electrochemical aptasensor was systematically characterized by EIS, DPV, and CV measurements in 5 mM $[Fe(CN)_6]^{3-/4-}$ and

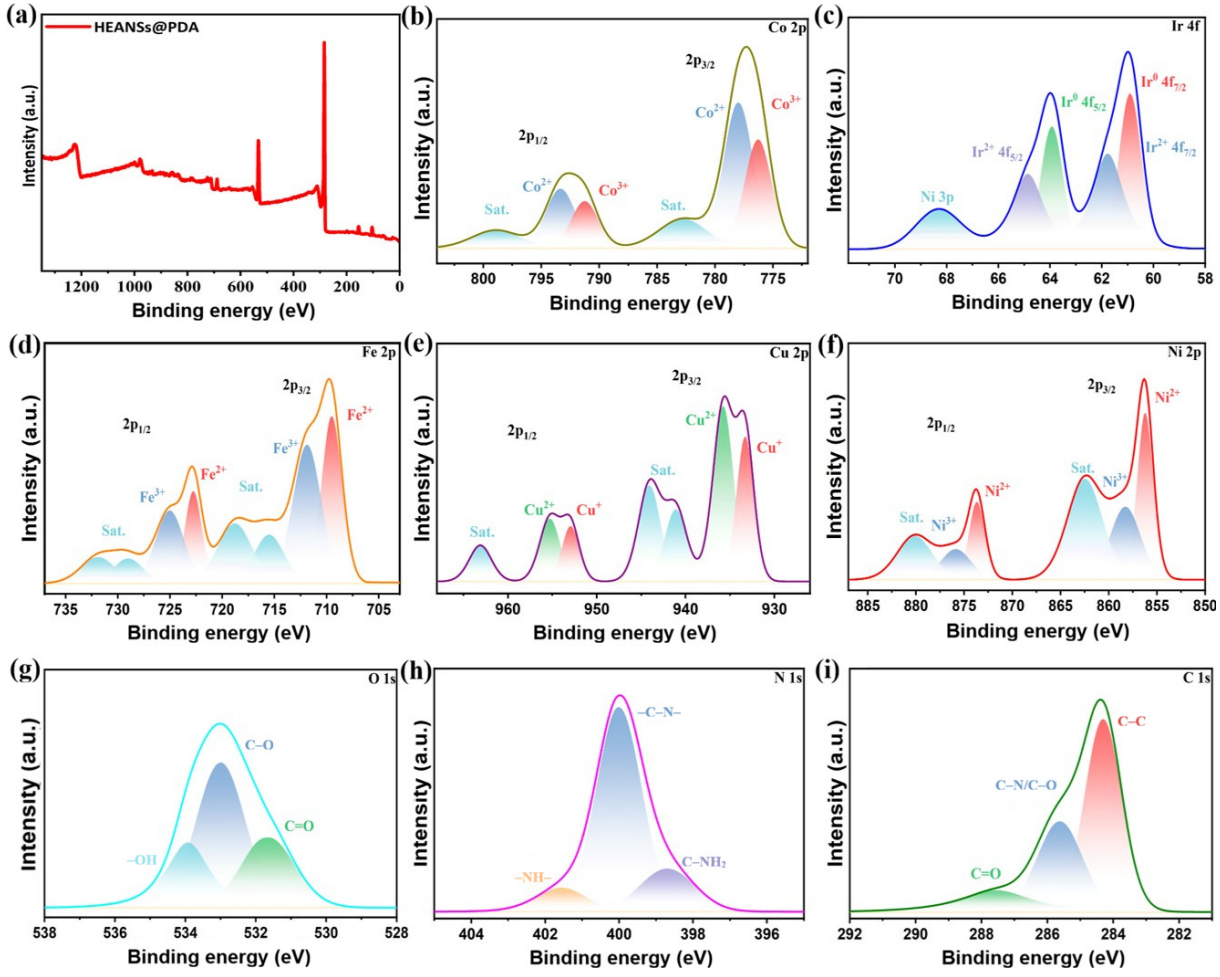

Figure 2 The XPS survey spectrum (a), along with high-resolution spectra of Co 2p (b), Ir 4f (c), Fe 2p (d), Cu 2p (e), Ni 2p (f), O 1s (g), N 1s (h), and C 1s (i), confirms the elemental composition and validates the successful PDA modification of the HEANSs surface.

0.1 M KCl. The BGCE displayed a pair of well-defined and reversible redox peaks corresponding to the $[Fe(CN)_6]^{3-/4-}$ redox couple (Fig. 3(a), curve (2)). Following the modification of GCE with HEANSs@PDA, a pronounced enhancement in the redox current was observed (Fig. 3(a), curve (1)). This increase in peak current highlights the excellent electrical conductivity of the nanostructure and verifies its successful deposition on the electrode surface, thereby facilitating efficient charge transport and accelerated electron transfer kinetics. The HEANSs served as a highly conductive and stable platform, while the PDA coating provided a conformal, adhesive layer enriched with abundant functional groups, enhancing interfacial electron mobility and offering versatile sites for efficient biomolecule binding. The modification of aptamer on the surface of HEANSs@PDA/GCE (Fig. 3(a), curve (3)) caused a measurable reduction in peak current, attributed to the inherently low conductivity of nucleic acids, which impedes charge transfer, and this process of bonding takes place by several interaction mechanisms, including (i) electrostatic attraction between positively charged surface groups of PDA-modified HEANSs and the negatively charged phosphate backbone of the aptamer, and (ii) hydrogen bonding between PDA's catechol/quinone groups and nucleobase functionalities. The highly porous structure of HEANSs@PDA provided a high density of reactive binding sites, enabling stable and uniform aptamer anchoring. Finally, exposure to ProGRP (10 ng/mL) resulted in an additional current drop (Fig. 3(a), curve (4)), confirming target binding, as the formation of a protein layer at the electrode interface further restricted electron transfer. EIS was used to probe interfacial charge transfer at each modification step. The Nyquist plots revealed a semi-circular region at high frequencies, representing charge transfer resistance (R_{ct}), and a linear region at low frequencies, corresponding to diffusion-controlled processes. Impedance measurements were conducted at an OCP of 0.27 mV to ensure equilibrium conditions. An equivalent circuit model comprising solution resistance (R_s), double-layer capacitance (C_{dl}), and R_{ct} was employed. Notably, an ideal capacitor was used in place of a constant phase element (CPE), owing to the high uniformity and low surface heterogeneity of the PDA-coated HEANSs electrode, which produced smooth semi-circular profiles. The R_{ct} of HEANSs@PDA/GCE (479.5 Ω, Fig. 3(b), curve (1)) was significantly lower than that of bare GCE (645.6 Ω, Fig. 3(b), curve (2)), underscoring the excellent conductivity of the nanocomposite. Immobilization of the aptamer raised Rct to 938.3 Ω (Fig. 3(b), curve (3)). After ProGRP binding, R_{ct} reached 1965.2 Ω (Fig. 3(b), curve (4)), demonstrating successful sensor assembly and sensitive detection capability.

This progressive R_{ct} increase aligns with Ohmic principles, as successive biomolecular layers hinder charge transfer, confirming efficient stepwise fabrication. The redox-active nature of HEANSs@PDA facilitated superior electron mobility, enabling rapid signal

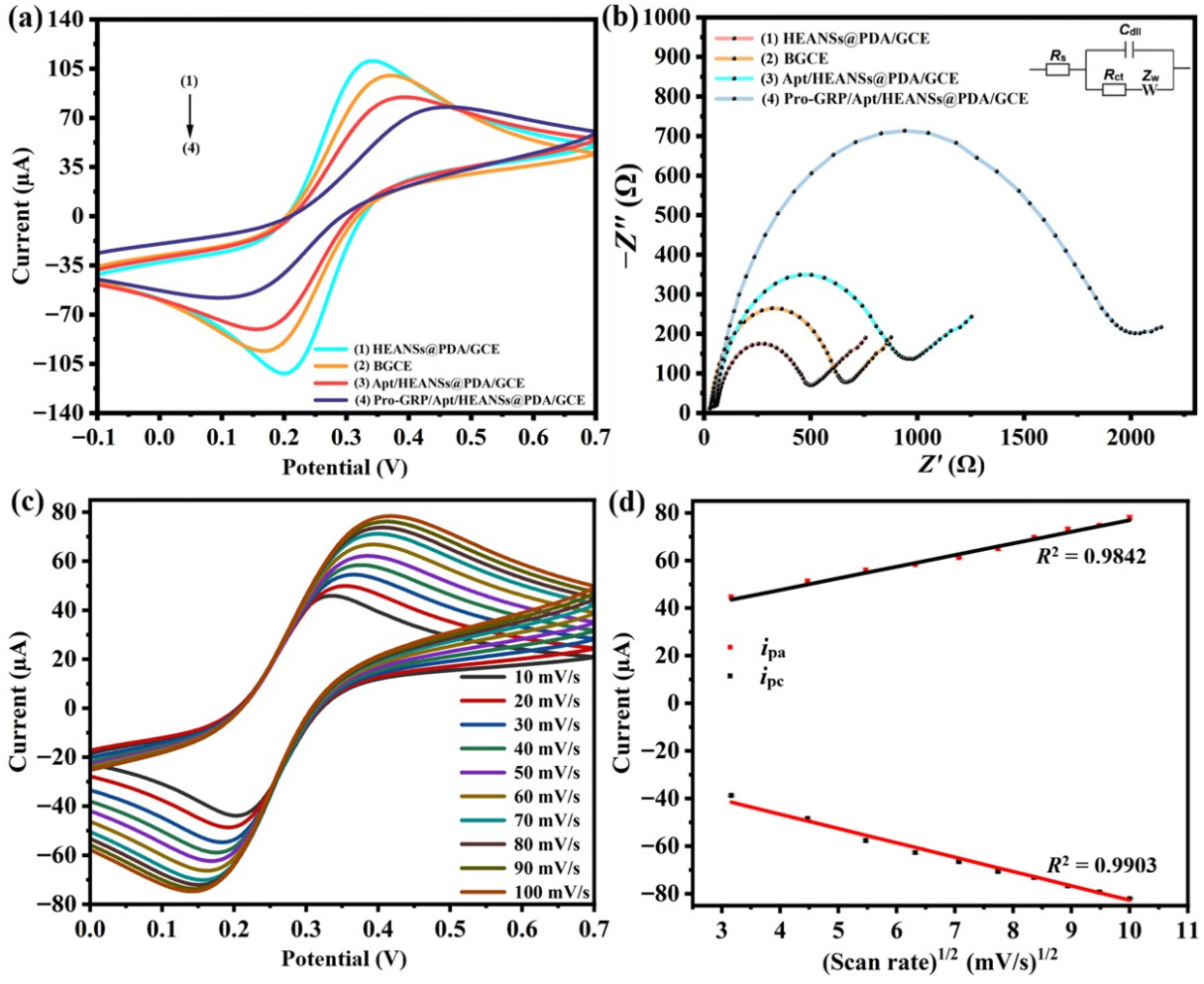

Figure 3 CV (a) and EIS Nyquist plots (b) for sequential electrode modification steps, (1) HEANSs@PDA/GCE, (2) BGCE, (3) Apt/HEANSs@PDA/GCE, and (4) ProGRP/Apt/HEANSs@PDA/GCE, along with CV responses of Apt/HEANSs@PDA/GCE at varying scan rates (c) and the corresponding linear relationship between redox peak currents and the square root of scan rate (d), confirming diffusion-controlled electron transfer in 0.10 M KCl with 5 mM $[Fe(CN)_6]^{3-/4-}$.

transduction during biomarker recognition. CV studies further supported the electrochemical properties of the sensor. The anodic and cathodic peak currents (i_{pa} and i_{pc}) increased linearly with the square root of the scan rate (10–100 mV/s), confirming a diffusion-controlled electrochemical process (Fig. 3(c)). The i_{pa}/i_{pc} ratio remained close to unity, confirming highly reversible redox behavior on the aptamer-functionalized surface (Fig. 3(d)). This synergy between conductive, catalytic HEANSs and recognition-enhancing PDA yields a robust and efficient aptasensor for ProGRP detection.

3.2 Optimization analysis of the fabricated aptasensor

To achieve maximum sensitivity, low background current, and reliable detection limits, the fabrication parameters of the electrochemical aptasensor were systematically optimized using DPV measurements (Fig. S2 in the ESM). Key optimization factors included the aptamer immobilization concentration, aptamer incubation time, and target biomarker (ProGRP) incubation time.

3.2.1 Determination of optimal aptamer concentration

HEANSs@PDA/GCE electrodes were incubated with varying concentrations of the ProGRP-specific aptamer (1.0–4.5 μM) for a fixed incubation period to evaluate the effect of aptamer loading on electrochemical response. As shown in Fig. 4(a), the DPV signal progressively decreased with increasing aptamer concentration due to the negatively charged phosphate backbone of the aptamer, which introduced significant electrostatic repulsion and steric hindrance to the redox probe ($[Fe(CN)_6]^{3-/4-}$), thereby impeding electron transfer at the electrode surface. A plateau was observed beyond 3.5 μM, suggesting surface saturation. Concentration lower than 3.5 μM left unoccupied binding sites, reducing recognition efficiency, whereas concentrations above 3.5 μM added minimal performance gains but increased nonspecific adsorption, leading to background noise. Therefore, 3.5 μM was selected as the optimal aptamer concentration for sensor assembly.

3.2.2 Optimization of aptamer immobilization time

The effect of immobilization of aptamer time was examined by modified HEANSs@PDA/GCE in a 3.5 μM aptamer solution for 5–45 min. The DPV current gradually decreased with increased immobilization time due to denser aptamer coverage, which hindered charge transport (Fig. 4(b)). After approximately 35 min, the current stabilized, indicating surface saturation and strong aptamer binding. Thus, 35 min was determined as the optimal aptamer immobilization time, balancing high coverage and minimized signal suppression.

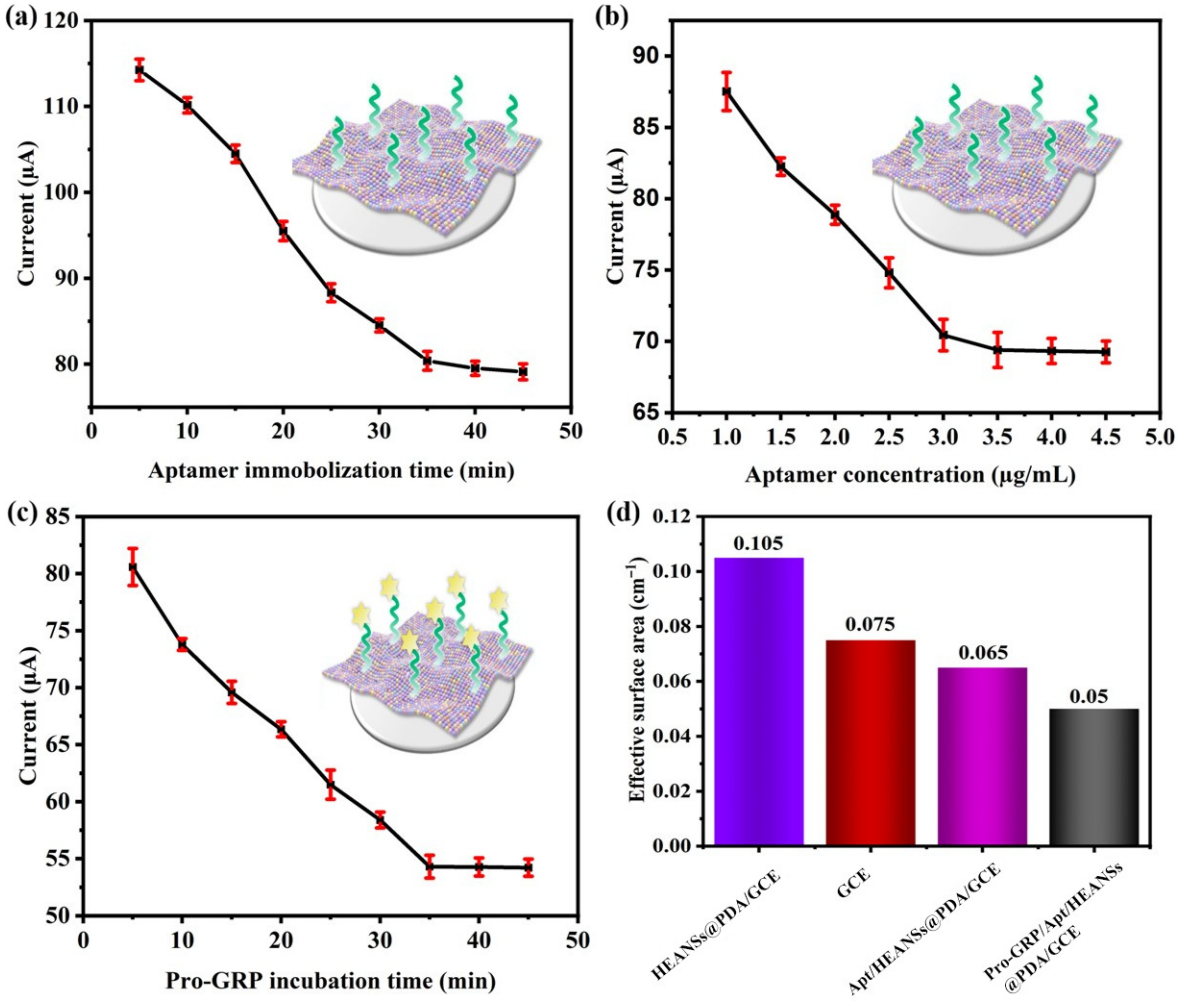

Figure 4 DPV analysis showing the influence of aptamer concentration (a), aptamer incubation time (b), ProGRP concentration (c), and corresponding changes in the effective electrode surface area (d) on the modification of the fabricated aptasensor.

3.2.3 Effect of ProGRP incubation time

To optimize target recognition, Apt/HEANSs@PDA/GCE electrodes were incubated with 10 ng/mL ProGRP (ProGRP/Apt/HEANSs@PDA/GCE) solutions for varying times (5–45 min). A notable reduction in current response was observed up to ~ 40 min (Fig. 4(c)), attributed to complete target aptamer binding and subsequent blocking of electron transfer pathways. Prolonged incubation yielded negligible changes, confirming equilibrium binding. Therefore, 40 min was selected as the optimal ProGRP incubation time for sensitive detection.

3.2.4 Effective surface area of electrodes

The effective surface area of each electrode was determined using the Randles–Sevcik equation, confirming successful stepwise sensor fabrication (Fig. 4(d)). The bare GCE exhibited a small surface area of 0.075 cm^2, consistent with its smooth, unmodified surface. After modification with HEANSs@PDA/GCE, the surface area increased significantly to 0.105 cm^2, attributed to the mesoporous, ultrathin structure surface of HEANSs@PDA, which provides abundant electroactive sites and improved surface roughness. Subsequent aptamer immobilization (Apt/HEANSs@PDA/GCE) reduced the surface area to 0.065 cm^2, reflecting the formation of a dense, non-conductive biomolecular layer that partially blocked electron transfer. Finally, ProGRP binding (ProGRP/Apt/HEANSs @PDA/GCE) further decreased the effective surface area to 0.050 cm^2, demonstrating successful target capture and confirming the aptasensor's stepwise assembly. This progressive trend highlights the role of HEANSs in enhancing electroactivity, PDA in providing functional anchoring sites for aptamer immobilization, and ProGRP binding in achieving high selectivity and sensitivity.

3.3 Reproducibility, stability, and selectivity analysis of sensor

To assess the reproducibility of the fabricated aptasensor (Fig. S3 in the ESM), five independently prepared electrodes were evaluated under optimized conditions for the detection of ProGRP at a concentration of 10 ng/mL (Fig. 5(a)). The recorded peak current responses exhibited an RSD of 1.78%, highlighting the excellent fabrication consistency and reliability of the sensor design. The stability of the aptasensor was further validated by storing the electrodes at 4 °C for nine days and re-evaluating their electrochemical response under identical conditions (Fig. 5(b)). A marginal signal decrease of only 3.752% compared to the initial measurements demonstrated that the aptasensor maintained its performance over prolonged storage, confirming its robust stability.

The selectivity of the sensor was rigorously investigated by

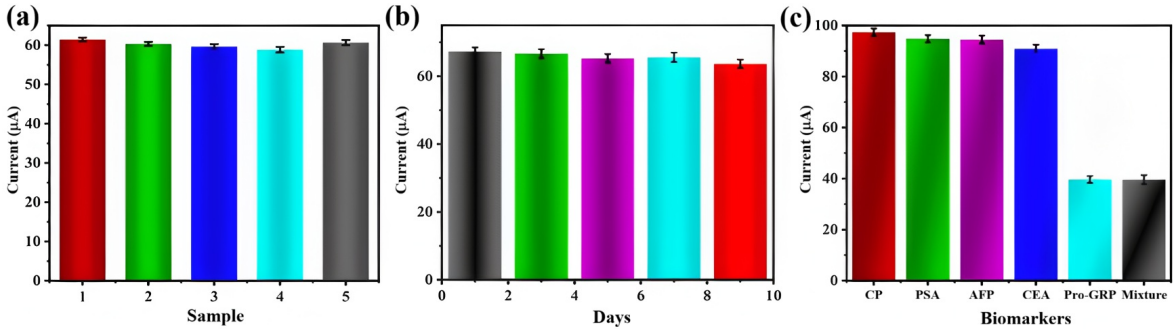

Figure 5 Electrochemical performance of the aptasensor demonstrating reproducibility using five independently fabricated sensors at 10 ng/mL ProGRP (a), stability after nine days of storage at 4 °C (b), and selectivity in the presence of potentially interfering cancer biomarkers (c).

monitoring its response in the presence of potentially interfering biomarkers, including AFP (200 ng/mL), PSA (200 ng/mL), CEA (200 ng/mL), CP (200 ng/mL), and 10 ng/mL of ProGRP (Fig. 5(c)). A control experiment using a mixture of these interfering proteins was also performed to ensure a rigorous evaluation (200 ng/mL of AFP, PSA, CEA, CP, and 10 ng/mL of ProGRP). The current response to ProGRP remained significantly distinguishable and nearly unaffected by the presence of high concentrations of other biomolecules, underscoring the aptasensor's high specificity. The selectivity of the aptasensor is primarily governed by the strong binding affinity between the aptamer and ProGRP, further enhanced by the large surface area and superior electrical conductivity of the HEANSs@PDA nanostructure. Additionally, the functional groups introduced through PDA coating provide a biocompatible interface that promotes robust and stable immobilization of the aptamer, thereby improving recognition specificity. These synergistic features enable ultrasensitive and reliable ProGRP detection in complex biological matrices, underscoring its potential for early cancer diagnostics.

3.4 Electrochemical sensing of ProGRP in serum samples

Accurate analysis of human serum samples is critical for evaluating the performance of electrochemical biosensors. To assess the practical applicability of the proposed electrochemical aptasensor, the ProGRP concentration in an untreated human serum sample was initially quantified as 0.25 ng/mL using a standard ELISA assay. Subsequently, the standard addition method was employed to determine the recovery efficiency of ProGRP in serum samples spiked with known concentrations (Table S1 in the ESM). The calculated recovery rates ranged from 96.8% to 98.0%, confirming the high accuracy of the developed sensor. Additionally, the RSD values, ranging from 2.4% to 3.2%, demonstrate excellent reproducibility and precision. These findings highlight the aptasensor's exceptional analytical performance, demonstrating high sensitivity, strong selectivity, robust stability, and reliable reproducibility, thereby supporting its potential for clinical diagnostic uses.

3.5 Sensing efficiency of the sensor

The fabricated electrochemical aptasensor was employed to quantify ProGRP under optimized conditions. As shown in Fig. 6(a), the DPV responses showed a progressive decrease in peak current as the ProGRP concentration increased from 10 pg/mL to 100 μg/mL. This attenuation in the DPV signal is attributed to the surface-blocking effect, whereby the specific binding of ProGRP to its immobilized aptamer forms a steric barrier on the electrode surface. The resulting biorecognition layer obstructs the access of the redox probe to the electrode interface, impeding its diffusion and thereby suppressing electron-transfer kinetics

a strong linear correlation between the peak current and the logarithm of ProGRP concentration was obtained (Fig. 6(b)), yielding the regression equation: $Y = (27.177 \pm 1.153) + (6.625 \pm 0.216) \times X$, with an excellent correlation coefficient ($R^2 = 0.9925$), confirming high linearity across the tested range. The calculated LOD was 0.874 pg/mL (S/N = 3), indicating the sensor's superior sensitivity. The remarkable sensing performance can be attributed to the unique characteristics of HEANSs@PDA. The multimetallic synergy of HEANSs provides high electrical conductivity, rapid electron-transfer kinetics, and abundant electroactive sites, while their mesoporous nanosheet morphology exposes a large accessible surface for biomolecular interactions. PDA functionalization further contributes by offering dense functional groups that enhance aptamer immobilization, improve biocompatibility, and increase antifouling properties. This dual functionality ensures both high sensitivity and superior selectivity. The detection mechanism relies on the specific aptamer–ProGRP interaction. In the absence of ProGRP, the redox probe readily accesses the HEANSs@PDA-modified electrode, producing a high current response owing to the excellent conductivity of the material. The binding of ProGRP forms bulky aptamer–target complexes that hinder electron transfer, leading to a concentration-dependent decrease in current. The HEANSs@PDA hybrid thus enables ultrasensitive ProGRP detection and highlights HEANSs-based nanostructures as versatile platforms for next-generation electrochemical biosensing and precision diagnostics. The comparative study is given (Table S2 in the ESM).

3.6 Control analysis and stability of the sensor

To confirm the specificity and biorecognition efficiency of the HEANSs@PDA-based electrochemical aptasensor for ProGRP detection, a series of control experiments was carried out using CV (Fig. S4 in the ESM). First, the GCE was modified with HEANSs@PDA (Fig. S4(a), curve (1) in the ESM). The 20 μL of BSA (0.02%) were deposited drop-wise on HEANSs@PDA/GCE, producing the BSA/HEANSs@PDA/GCE (Fig. S4(a), curve (2) in the ESM). To investigate whether ProGRP could directly adsorb to the electrode surface without aptamer functionalization, 20 μL of ProGRP solution (10 ng/mL) was introduced to the BSA/HEANSs @PDA/GCE, forming ProGRP/BSA/HEANSs@PDA/GCE. The CV response (Fig. S4(a), curve (3) in the ESM) showed a negligible change in current density, indicating minimal nonspecific adsorption of ProGRP. After that aptamer functionalization, 8 μL of a (3.5 μM) aptamer was drop-cast onto the HEANSs@PDA/GCE

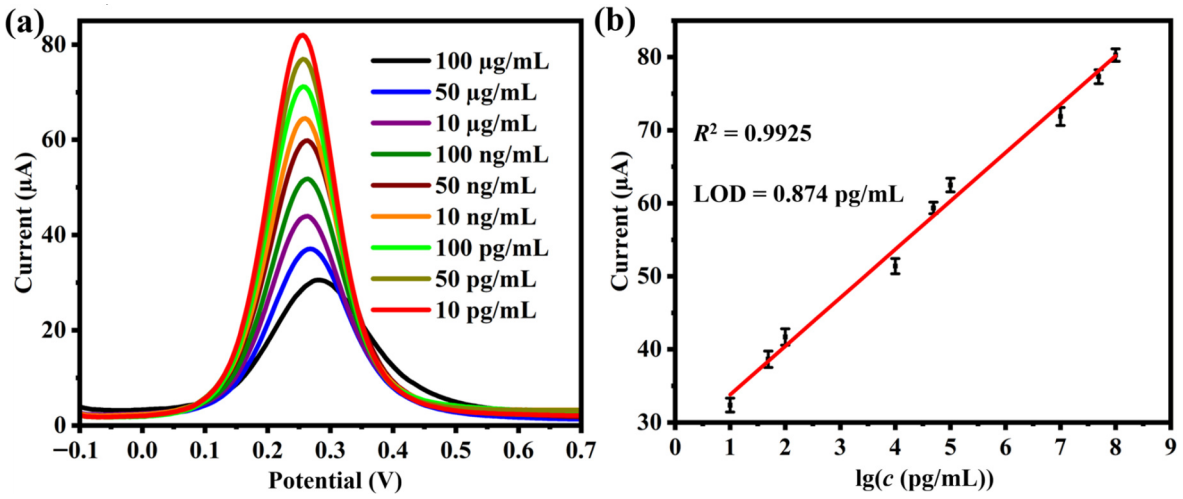

Figure 6 DPV responses of the Apt/HEANSs@PDA/GCE aptasensor toward varying ProGRP concentrations (a) and the corresponding calibration curve illustrating the sensor's quantitative detection performance (b).

surface to form Apt/HEANSs@PDA/GCE and analyzed, and a noticeable decrease in peak current was observed (Fig. S4(a), curve (4) in the ESM), attributed to the negatively charged aptamer hindering electron transfer. Finally, to evaluate target recognition, 20 μL of ProGRP (10 ng/mL) was incubated on the Apt/HEANSs@PDA/GCE, followed by a further decline in current density, confirming specific ProGRP binding to the immobilized aptamer-based modified electrode (Fig. S4(a), curve (5) in the ESM). These findings demonstrate that ProGRP binding in the absence of an aptamer does not significantly alter the electrochemical response, whereas aptamer functionalization enables highly specific target recognition, validating the strong specificity and reliable biorecognition performance of the developed aptasensor. The stability of the electrochemical biosensor was evaluated by CV over 50 cycles (Fig. S4(b) in the ESM). The nearly identical responses observed in the first (1st) (Fig. S4(b), curve (1) in the ESM) and fiftieth (50th) cycle (Fig. S4(b), curve (2) in the ESM) confirm the excellent stability of the fabricated sensor.

4 Conclusion

In conclusion, we developed a highly sensitive and selective electrochemical aptasensor based on HEANSs@PDA for the detection of ProGRP, a critical biomarker for SCLC. HEANSs were synthesized using a salt-templating approach, yielding ultrathin 2D nanosheets with abundant electroactive sites. In addition, PDA modification introduced dense functional groups that enhanced biocompatibility and improved aptamer immobilization efficiency. The multimetallic composition further exploits lattice distortion and synergistic effects to achieve superior catalytic activity, rapid electron transfer, and robust chemical stability. The resulting aptasensor demonstrated an ultra-low LOD of 0.874 pg/mL, a broad linear range of 10 pg/mL to 100 μg/mL, and excellent RSD 1.78% and stability, retaining over 3.75% of its initial signal after nine days. Furthermore, it exhibited remarkable selectivity against potential interfering biomarkers and achieved high recovery rates in human serum samples (96.8%–98.0%), underscoring its practical clinical applicability. This work not only represents the first integration of HEANSs@PDA based aptamer immobilization for ProGRP detection but also introduces a versatile, scalable, and high-performance platform, highlighting the unique multimetallic synergy of 2D HEANSs for next-generation, ultrasensitive cancer diagnostics and precision medicine applications.

Electronic Supplementary Material: Supplementary material (SEM-EDS mapping; DPV analysis of optimization study, including reproducibility, stability, selectivity, Aptamer concentration, aptamer incubation time, and ProGRP incubation time; CV study for the control experiments and stability; the analysis table in diluted human serum samples demonstrated high accuracy and reproducibility; a comparative analysis and references are included) is available in the online version of this article at https://doi.org/10.26599/NR.2026.94908352.

Data availability

All data needed to support the conclusions in the paper are presented in the manuscript and the Electronic Supplementary Material. Additional data related to this paper may be requested from the corresponding author upon request.

Acknowledgements

This work was financially supported by the Natural Science Foundation of Beijing (No. L256002), the National Key R&D Program of China (Nos. 2023YFC3504401 and 2022YFA1103403), the National Natural Science Foundation of China (Nos. 82574366, 82304442, and 22304099), and Innovation Team and Talents Cultivation Program of the National Administration of Traditional Chinese Medicine (Nos. ZYYCXTD-C-202401 and ZYYCXTD-D-202208).

The authors gratefully acknowledge the support and facilities provided by the Analysis Centre of Tsinghua University. We also express our sincere gratitude to the Natural Science Foundation of Beijing, the Ministry of Science and Technology, the National Natural Science Foundation of China, and the State Administration of Traditional Chinese Medicine for their generous support and funding.

Declaration of competing interest

All the contributing authors report no conflict of interests in this work.

Author contribution statement

I. C.: Data curation, validation, writing manuscript, experimental design. Y. J. A. and Q. L. L.: Writing – review & editing, project administration, supervision, funding acquisition, conceptualization. All the authors have approved the final manuscript.

Use of AI statement

None.

References

[1] Yao, L. G.; Li, Y. L.; Wang, Q.; Chen, T.; Li, J. Y.; Wang, Y. J.; Zhang, L. Y.; Su, L.; Li, L. Q.; Lou, Q. Q. et al. Multi-biomarkers panel in identifying benign and malignant lung diseases and pathological types of lung Cancer. *J. Cancer* **2023**, *14*, 1904–1912.

[2] Rosiek, V.; Kogut, A.; Kos-Kudła, B. Pro-gastrin-releasing peptide as a biomarker in lung neuroendocrine neoplasm. *Cancers* **2023**, *15*, 3282.

[3] Zhu, L.; Qin, J. Predictive biomarkers for immunotherapy response in extensive-stage SCLC. *J. Cancer Res. Clin. Oncol.* **2024**, *150*, 22.

[4] Zhou, D.; Byers, L. A.; Sable, B.; Smit, M. A. D.; Sadraei, N. H.; Dutta, S.; Upreti, V. V. Clinical pharmacology profile of AMG 119, the first chimeric antigen receptor T (CAR-T) cell therapy targeting delta-like ligand 3 (DLL3), in patients with relapsed/refractory small cell lung cancer (SCLC). *J. Clin. Pharmacol.* **2024**, *64*, 362–370.

[5] La'ah, A. S.; Chiou, S. H. Cutting-edge therapies for lung cancer. *Cells* **2024**, *13*, 436.

[6] Shang, X. L.; Zhang, C. Y.; Kong, R. H.; Zhao, C. L.; Wang, H. Y. Construction of a diagnostic model for small cell lung cancer combining metabolomics and integrated machine learning. *Oncologist* **2024**, *29*, e392–e401.

[7] Fu, F. Q.; Chen, Z. W.; Chen, H. Q. Treating lung cancer: Defining surgical curative time window. *Cell Res.* **2023**, *33*, 649–650.

[8] Cittolin-Santos, G. F.; Knapp, B.; Ganesh, B.; Gao, F.; Waqar, S.; Stinchcombe, T. E.; Govindan, R.; Morgensztern, D. The changing landscape of small cell lung cancer. *Cancer* **2024**, *130*, 2453–2461.

[9] Chandio, I.; Rahujo, S.; Chandio, Z. A.; Rashid, M. A.; Rehman, M. U.; Shar, Z. H.; Thebo, K. H. Recent development in metal-organic frameworks-based electrochemical aptasensors for detection of cancer biomarkers. *Bioelectrochemistry* **2025**, *165*, 109006.

[10] Li, M.; Han, D. D.; Wang, W.; Zhang, Y.; Li, D.; Dai, C. Y.; Qian, L. T.; Lin, W. C. Decline in serum progastrin-releasing peptide predicts the response of patients with small cell lung cancer to chemotherapy. *Oncol. Lett.* **2020**, *20*, 301.

[11] Mondelo-Macía, P.; García-González, J.; León-Mateos, L.; Castillo-García, A.; López-López, R.; Muinelo-Romay, L.; Díaz-Peña, R. Current status and future perspectives of liquid biopsy in small cell lung cancer. *Biomedicines* **2021**, *9*, 48.

[12] Killock, D. Liquid biopsy of SCLC chemosensitivity. *Nat. Rev. Clin. Oncol.* **2017**, *14*, 2.

[13] Fasano, R.; Serratì, S.; Rafaschieri, T.; Longo, V.; Di Fonte, R.; Porcelli, L.; Azzariti, A. Small-cell lung cancer: Is liquid biopsy a new tool able to predict the efficacy of immunotherapy. *Biomolecules* **2024**, *14*, 396.

[14] Wei, Z.; Cai, X. P.; Zhang, J. P.; Fan, J. M.; Xu, J. Y.; Xu, L. R. High sensitive immunoelectrochemical measurement of lung cancer tumor marker ProGRP based on TiO_2-Au nanocomposite. *Molecules* **2019**, *24*, 656.

[15] Wu, X. Y.; Hu, Y. B.; Li, H. J.; Wan, B.; Zhang, C. X.; Zhang, B.; Hu, H.; Zhang, Q.; Lv, T. F.; Zhan, P. et al. Diagnostic and therapeutic value of progastrin-releasing peptide on small-cell lung cancer: A Single-Center Experience in China. *J. Cell. Mol. Med.* **2018**, *22*, 4328–4334.

[16] Chandio, I.; Ai, Y. J.; Wu, L.; Liang, Q. L. Recent progress in MOFs-based nanozymes for biosensing. *Nano Res.* **2024**, *17*, 39–64.

[17] Banglani, T. H.; Chandio, I.; Khilji, M. U. N.; Ibrar, A.; Memon, A. A.; Ali, A.; Al-Anzi, B. S.; Thebo, K. H. Graphene-based nanocomposites for gas sensors: Challenges and opportunities. *Rev. Inorg. Chem.* **2024**, *44*, 385–408.

[18] Huang, Z.; Xu, D.; Zhang, F.; Ying, Y.; Song, L. Pro-gastrin-releasing peptide and neuron-specific enolase: Useful predictors of response to chemotherapy and survival in patients with small cell lung cancer. *Clin. Transl. Oncol.* **2016**, *18*, 1019–1025.

[19] Winther, B.; Reubsaet, J. L. Determination of the small cell lung cancer associated biomarker pro-gastrin-releasing peptide (ProGRP) using LC-MS. *J. Sep. Sci.* **2007**, *30*, 234–240.

[20] Li, L.; Chen, Z. B. Electrochemical aptamer biosensor for DNA detection based on label-free aptamers. *Bioelectrochemistry* **2023**, *153*, 108494.

[21] Rozi, N.; Hanifah, S. A.; Abd Karim, N. H.; Heng, L. Y.; Higashi, S. L.; Ikeda, M. Enhancing electrochemical biosensor performance for 17β-estradiol determination with short split—aptamers. *Biosensors* **2022**, *12*, 1077.

[22] Cao, F. J.; Feng, H.; Yao, J. X.; Hou, X.; Jin, T. Z.; Hui, J. F. Rapid synthesis of oxygen-defected molybdenum oxides quantum dots as efficient nanozymes for healing diabetic ulcers. *Nano Res.* **2024**, *17*, 6376–6385.

[23] Meng, H. M.; Liu, H.; Kuai, H. L.; Peng, R. Z.; Mo, L. T.; Zhang, X. B. Aptamer-integrated DNA nanostructures for biosensing, bioimaging and cancer therapy. *Chem. Soc. Rev.* **2016**, *45*, 2583–2602.

[24] Zou, Y. N.; Su, Y. Y.; Yu, Y. C.; Luo, J. L.; Kang, X. M.; Zhang, J.; Lan, L. H.; Wang, T. S.; Li, J. On the role of Zn and Fe doping in nitrogen-carbon electrocatalysts for oxygen reduction. *Nano Res.* **2024**, *17*, 9564–9572.

[25] Feng, F.; Zhang, Y. H.; Zhang, X.; Mu, B.; Zhang, J. H.; Qu, W. J.; Tong, W. S.; Liang, M. M.; An, Q.; Guo, Z. J. et al. Enhancing the peroxidase-like activity of MoS_2-based nanozymes by introducing attapulgite for antibacterial application and sensitive detection of glutathione. *Nano Res.* **2024**, *17*, 7415–7426.

[26] Ellington, A. D.; Szostak, J. W. *In vitro* selection of RNA molecules that bind specific ligands. *Nature* **1990**, *346*, 818–822.

[27] Kissmann, A. K.; Bolotnikov, G.; Li, R. L.; Müller, F.; Xing, H.; Krämer, M.; Gottschalk, K. E.; Andersson, J.; Weil, T.; Rosenau, F. IMPATIENT-qPCR: Monitoring SELEX success during *in vitro* aptamer evolution. *Appl. Microbiol. Biotechnol.* **2024**, *108*, 284.

[28] Qi, S.; Duan, N.; Khan, I. M.; Dong, X. Z.; Zhang, Y.; Wu, S. J.; Wang, Z. P. Strategies to manipulate the performance of aptamers in SELEX, post-SELEX and microenvironment. *Biotechnol. Adv.* **2022**, *55*, 107902.

[29] Li, H. H.; Hu, W. W.; Hassan, M. M.; Zhang, Z. Z.; Chen, Q. S. A facile and sensitive SERS-based biosensor for colormetric detection of acetamiprid in green tea based on unmodified gold nanoparticles. *J. Food Meas. Charact.* **2019**, *13*, 259–268.

[30] Li, Y. F.; Wang, W. D.; Yue, W. X.; Lei, Q.; Zhao, Z. T.; Sun, Y. J.; Xu, H. Y.; Zhang, W. D.; Chen, L.; Kim, J. K. et al. Construction of highly sensitive electrochemical immunosensor based on Au and Co_3O_4 nanoparticles functionalized Ni/Co bimetal conductive MOF for quantitative detection of HBsAg. *Chem. Eng. J.* **2024**, *483*, 149087.

[31] Manoharan, A. K.; Batcha, M. I. K.; Mahalingam, S.; Raj, B.; Kim, J. Recent advances in two-dimensional nanomaterials for healthcare monitoring. *ACS Sens.* **2024**, *9*, 1706–1734.

[32] Chandio, I.; Cheung, S.; Ai, Y. J.; Liang, Q. L. High-entropy alloy nanoparticles integrated with metal-organic framework for enhanced aptasensing of carcinoembryonic antigen. *Microchem. J.* **2025**, *209*, 112760.

[33] Chandio, I.; Cheung, S.; Wu, L.; Cui, M. Y.; Ai, Y. J.; Liang, Q. L. Engineered rGO-AuNPs@MXene hybrid nanocomposites for highly

efficient electrochemical aptasensing of alpha-fetoprotein. *Microchem. J.* **2025**, *214*, 113952.
[34] Chandio, I.; Jiao, Q. S.; Li, R. Q.; Ai, Y. J.; Liang, Q. L. Dual-signal electrochemical aptasensor based on high-entropy alloy nanosheets for calprotectin detection in inflammatory bowel disease. *ACS Appl. Mater. Interfaces* **2025**, *17*, 38960–38970.
[35] Pang, M. Y.; Yang, M.; Zhang, H. H.; Shen, Y. Q.; Kong, Z.; Ye, J. J.; Shan, C. Y.; Wang, Y.; An, J.; Li, W. S. et al. Synthesis techniques, mechanism, and prospects of high-loading single-atom catalysts for oxygen reduction reactions. *Nano Res.* **2024**, *17*, 9371–9396.
[36] Nandan, R.; Raj, G.; Nanda, K. K. FeCoNiMnCr high-entropy alloy nanoparticle-grafted NCNTs with promising performance in the ohmic polarization region of fuel cells. *ACS Appl. Mater. Interfaces* **2022**, *14*, 16108–16116.
[37] Zhang, W. J.; Feng, X.; Mao, Z. X.; Li, J.; Wei, Z. D. Stably immobilizing sub-3 nm high-entropy Pt alloy nanocrystals in porous carbon as durable oxygen reduction electrocatalyst. *Adv. Funct. Mater.* **2022**, *32*, 2204110.
[38] Jia, Z.; Yang, Y. Y.; Wang, Q.; Kong, C.; Yao, Y.; Wang, Q. Q.; Sun, L. G.; Shen, B. L.; Kruzic, J. J. An ultrafast and stable high-entropy metallic glass electrode for alkaline hydrogen evolution reaction. *ACS Mater. Lett.* **2022**, *4*, 1389–1396.
[39] Wang, Y.; Ma, F. Y.; Zhang, G. Q.; Zhang, J. W.; Zhao, H.; Dong, Y. M.; Wang, D. S. Precise synthesis of dual atom sites for electrocatalysis. *Nano Res.* **2024**, *17*, 9397–9427.
[40] Nguyen, T. X.; Su, Y. H.; Lin, C. C.; Ruan, J.; Ting, J. M. A new high entropy glycerate for high performance oxygen evolution reaction. *Adv. Sci.* **2021**, *8*, 2002446.
[41] Tao, L.; Sun, M. Z.; Zhou, Y.; Luo, M. C.; Lv, F.; Li, M. G.; Zhang, Q. H.; Gu, L.; Huang, B. L.; Guo, S. J. A general synthetic method for high-entropy alloy subnanometer ribbons. *J. Am. Chem. Soc.* **2022**, *144*, 10582–10590.
[42] Xu, H. D.; Zhang, Z. H.; Liu, J. X.; Do-Thanh, C. L.; Chen, H.; Xu, S. H.; Lin, Q. J.; Jiao, Y.; Wang, J. L.; Wang, Y. et al. Entropy-stabilized single-atom Pd catalysts via high-entropy fluorite oxide supports. *Nat. Commun.* **2020**, *11*, 3908.
[43] Gu, Z. Y.; Guo, J. Z.; Cao, J. M.; Wang, X. T.; Zhao, X. X.; Zheng, X. Y.; Li, W. H.; Sun, Z. H.; Liang, H. J.; Wu, X. L. An advanced high-entropy fluorophosphate cathode for sodium-ion batteries with increased working voltage and energy density. *Adv. Mater.* **2022**, *34*, 2270110.
[44] Luan, H. W.; Zhang, X.; Ding, H. Y.; Zhang, F.; Luan, J. H.; Jiao, Z. B.; Yang, Y. C.; Bu, H. T.; Wang, R. B.; Gu, J. L. et al. High-entropy induced a glass-to-glass transition in a metallic glass. *Nat. Commun.* **2022**, *13*, 2183.
[45] McCormick, C. R.; Schaak, R. E. Simultaneous multication exchange pathway to high-entropy metal sulfide nanoparticles. *J. Am. Chem. Soc.* **2021**, *143*, 1017–1023.
[46] Ai, Y. J.; He, M. Q.; Sun, H.; Jia, X. M.; Wu, L.; Zhang, X. Y.; Sun, H. B.; Liang, Q. L. Ultra-small high-entropy alloy nanoparticles: Efficient nanozyme for enhancing tumor photothermal therapy. *Adv. Mater.* **2023**, *35*, 2302335.
[47] Zhang, X. L.; Tao, C. Y.; Chu, S. S.; Liu, W. D.; Xia, M. Y.; Jiang, Y. Y.; Lu, Y. Z. Single cobalt sites on defective carbon nanosheets as efficient oxidase mimics for visual biosensing. *Nano Res.* **2025**, *18*, 94907336.
[48] Zmerli, I.; Michel, J. P.; Makky, A. Bioinspired polydopamine nanoparticles: Synthesis, nanomechanical properties, and efficient PEGylation strategy. *J. Mater. Chem. B* **2020**, *8*, 4489–4504.
[49] Ye, M. Y.; Su, T. T.; Li, J.; Chen, X. W.; Ying, D. C.; Wu, S. J.; Wang, Z. P.; Duan, N. Multifunctional Ce-MOF@PdNPs with colorimetric fluorescent electrochemical activity for ultrasensitive and accurate detection of diethylstilbestrol. *Nano Res.* **2024**, *17*, 9990–9998.
[50] Hong, F. F.; Li, Y. J.; Zhou, X.; Zhu, X. Y.; Zhai, Y. Z.; Yang, C. X.; Huang, Q.; Chen, L.; Lu, Y.; Wang, L. et al. Recent advances for medium-and high-entropy based layered cathodes for sodium ion batteries. *Nano Res. Energy* **2025**, *4*, e9120185.
[51] Sun, Y. F.; Dai, S. High-entropy materials for catalysis: A new frontier. *Sci. Adv.* **2021**, *7*, eabg1600.
[52] Ai, Y. J.; Wang, Z. Y.; Shi, W. H.; Jia, X. M.; Cui, M. Y.; Sun, H. B.; Ren, F. Z.; He, M. Q.; Liang, Q. L. Atomic-level high-entropy nanozymes enable remarkable endogenous targeted catalysis and enhancing tumor photothermal therapy. *Adv. Mater.* **2025**, *37*, 2502322.
[53] Jin, T.; Sang, X. H.; Unocic, R. R.; Kinch, R. T.; Liu, X. F.; Hu, J.; Liu, H. L.; Dai, S. Mechanochemical-assisted synthesis of high-entropy metal nitride via a soft urea strategy. *Adv. Mater.* **2018**, *30*, 1707512.
[54] Wei, H. H.; Wang, Q.; Zhang, Y.; Li, J.; Liu, P.; Wang, N. N.; Gong, X. Q. Engineering high-entropy alloy nanosheets toward efficient electrocatalytic water oxidation. *Fuel* **2024**, *358*, 130011.
[55] Mie, M.; Kai, T.; Le, T.; Cass, A. E. G.; Kobatake, E. Selection of DNA aptamers with affinity for pro-gastrin-releasing peptide (proGRP), a tumor marker for small cell lung cancer. *Appl. Biochem. Biotechnol.* **2013**, *169*, 250–255.
[56] He, M. Q.; An, M. Y.; Wang, Z. Y.; Lin, C. S.; Shi, W. H.; Sun, H. B.; Ren, F. Z.; Liang, Q. L.; Ai, Y. J. Ultra-small medium-entropy nanozymes for targeting catalysis therapy of tumor. *Chem. Eng. J.* **2025**, *526*, 170863.
[57] Amiri, A.; Shahbazian-Yassar, R. Recent progress of high-entropy materials for energy storage and conversion. *J. Mater. Chem. A* **2021**, *9*, 782–823.
[58] Bolar, S.; Ito, Y.; Fujita, T. Future prospects of high-entropy alloys as next-generation industrial electrode materials. *Chem. Sci.* **2024**, *15*, 8664–8722.
[59] Lin, C. S.; Shi, W. H.; Zhu, Y. F.; Ma, W. H.; Ai, Y. J.; Wang, J.; Liang, Q. L.; He, M. Q. Atomic iron-engineered dual-modal nanozyme enhances tumor-targeted chemodynamic/photothermal synergistic therapy. *Nano Res.*, in press, DOI: 10.26599/NR.2025.94908256.

This is an open access article under the terms of the Creative Commons Attribution 4.0 International License (CC BY 4.0, https://creativecommons.org/licenses/by/4.0/).

© The Author(s) 2026. Published by Tsinghua University Press.